Two-Way Linked Multiscale Method Integrated with Nanomechanical Tests and Cohesive Zone Fracture to Model Highly Heterogeneous Binding Materials

Keyvan Zare Rami[1]; Yong-Rak Kim, M.ASCE[2]; Mahdieh Khedmati[3]; Gabriel Nsengiyumva[4]; and Hani Alanazi[5]

Abstract: This paper presents a two-way linked multiscale method that is integrated with nanomechanical tests and a cohesive zone fracture model to investigate highly heterogeneous cementitious materials such as alkali-activated geopolymer. To this end, geopolymer paste, which is known to have multiphase heterogeneous media, was fabricated and tested to identify (1) local-scale microstructures and nanomechanical properties of individual components within the paste, and (2) global-scale fracture through a three-point bending beam test. Local–global results were then integrated with the two-way linked finite-element modeling. Global and local scales were systemically represented in the model with a homogeneous bending beam structure where the elements of the potential crack zone are linked to a heterogeneous geopolymer microstructure representative volume element (RVE) in the two-way coupled multiscale modeling framework. This integrated experimental–computational multiscale approach can provide the material properties, such as micrometer-length-scale cohesive zone fracture properties, which are considered core properties but not usually feasible to identify using conventional test methods. Test-modeling results imply that the two-way linked multiscale method integrated with nanomechanical tests can be used as a method for characterization and design of various multiphase media, including materials used for critical civil infrastructure. **DOI: 10.1061/(ASCE)EM.1943-7889.0001518.**

Author keywords: Two-way linked multiscale model; Nanomechanical properties; Alkali-activated geopolymer; Cohesive zone fracture.

Introduction

The study of material performance and behavior is usually performed solely on a single-length scale at which the material can be approximated as a homogeneous medium. However, the material's overall response is most likely influenced by multiple-length scale mechanisms acting upon the microstructural heterogeneity existing in the material. Therefore, through adequate understanding of the smaller-length scale, the complex behavior of a heterogeneous material can be estimated in a more accurate and physically representative manner. Smaller-scale investigations include a mixture microstructure where the different phases are distinguishable and the properties of individual phases are interrelated. Smaller-scale properties of different phases can then be homogenized to estimate the overall effective properties of larger-scale bodies through the micromechanics concept (Hill 1972; Hashin 1983; Broughton et al. 1999; Allen 2001). In combination with numerical approaches, the linking between length scales can be achieved more efficiently, particularly for objects with complex geometries and microstructural characteristics. Many studies have challenged such complex issues through different modeling approaches, including the two-way coupled multiscale computational modeling method (Souza et al. 2008; Souza and Allen 2010; Kim et al. 2013; You et al. 2017).

In the field of civil infrastructural materials, various cementitious binding materials such as portland cement paste and geopolymer paste are known to have multiphase microstructures in several length scales. Owing to the recent advancement in microscale and nanoscale experimental technology, these materials have been studied extensively in order to investigate and characterize their multiscale properties. The microstructural characteristics of multiphase portland cement concrete and geopolymer concrete paste have been determined using various tests, such as imaging analyses by scanning electron microscopy (SEM) (Bleszynski and Thomas 1998; Mouret et al. 1999; Winnefeld et al. 2010), chemical mapping by energy dispersive spectroscopy (EDS), physical phase mapping by atomic force microscopy (AFM) (Trtik et al. 2012), or a combination of these techniques with additional supportive tests (Bakharev 2005; Lecomte et al. 2006; Škvára et al. 2006; Winnefeld et al. 2010; Somna et al. 2011; Shi et al. 2012; Das et al. 2015; Allison et al. 2015; Khedmati et al. 2018). Some studies have used the nanoindentation method to characterize the elastic and viscoelastic properties of fly ash–based geopolymer paste (Sakulich and Li 2011; Mondal et al. 2008; Němeček 2009; Němeček et al. 2009, 2011; Menčík et al. 2011; Pelisser et al. 2013; Da Silva et al. 2014; Allison et al. 2015; Das et al. 2015). The overall homogenized elastic moduli of concrete paste were approximated by using the homogenization method (Hain and Wriggers 2008; Šmilauer et al. 2011; Das et al. 2015). Qian et al. (2011) simulated the three-dimensional (3D) fracture of cement

[1]Ph.D. Student, Dept. of Civil Engineering, Univ. of Nebraska-Lincoln, Lincoln, NE 68588.

[2]Professor, Dept. of Civil Engineering, Univ. of Nebraska-Lincoln, Lincoln, NE 68588 (corresponding author). Email: yong-rak.kim@unl.edu

[3]Ph.D. Student, Dept. of Civil Engineering, Univ. of Nebraska-Lincoln, Lincoln, NE 68588.

[4]Ph.D. Student, Dept. of Civil Engineering, Univ. of Nebraska-Lincoln, Lincoln, NE 68588.

[5]Ph.D. Student, Dept. of Civil Engineering, Univ. of Nebraska-Lincoln, Lincoln, NE 68588.

Note. This manuscript was submitted on September 12, 2017; approved on April 30, 2018; published online on July 31, 2018. Discussion period open until December 31, 2018; separate discussions must be submitted for individual papers. This paper is part of the ***Journal of Engineering Mechanics***, © ASCE, ISSN 0733-9399.

paste at microscale using a lattice model. Nguyen et al. (2012) and others have extended this approach and studied the failure of hardened cement paste using a numerical multiscale framework based on microscale component properties (Nguyen et al. 2012; Karamnejad et al. 2013; Karamnejad and Sluys 2014). Although these attempts have provided opportunities to analyze the fracture behavior of heterogeneous materials more accurately based on the smaller-scale properties, they also have consequential challenges, such as difficulties/limitations in identification of microscale fracture properties, because typical test methods are certainly limited to identify these properties directly.

To overcome these limitations, an alternative approach is necessary to account for microscale fracture of mixture components without the need for small-scale fracture testing, which is mostly not experimentally feasible. The approach should still be based on scientific rigor. To this end, this study attempts to address the challenges with a hypothesis postulating that an integrated experimental–computational multiscale modeling method can identify the microscale fracture properties of heterogeneous media, including cementitious pastes. To test the hypothesis, multiscale tests (local-scale tests for component properties and global-scale tests of mixture behavior) and the two-way coupled computational modeling were conducted and integrated.

Study Objectives and Methodology

In this study, a multiscale experimental–computational framework is used to account for the microscale fracture of mixture components without the need for small-scale fracture testing. Our modeling approach was applied to a widely used infrastructure material, namely geopolymer binding paste, as an example case. The geopolymer paste is known to have a highly heterogeneous nature in the small-scale microstructure owing to the interaction of many different ingredients. The primary objectives of this study are as follows:

- Develop a two-way coupled finite-element multiscale model for simulating the failure of geopolymer paste by allowing development of microcracks in the paste microstructure.
- Identify microstructural characteristics and mechanical properties of individual phases in the microstructure through multiscale experiments.
- Apply the computational two-way linked multiscale modeling to the geopolymer paste to identify and calibrate unknown fracture properties at the micrometer length scale.

To meet these objectives, a three-point bending beam test was conducted as a global-scale fracture test of geopolymer paste specimens, and the microstructural characteristics and nanomechanical properties of the individual phases in the geopolymer paste were directly determined using a series of microstructure imaging and nanoindentation tests as local-scale measurements. Test results from the two length scales (i.e., global and local) were then integrated with the two-way linked multiscale computational modeling and simulations in order to identify the unknown fracture properties within the geopolymer paste. This modeling approach is expected to provide new insight and to help in understanding the contribution of material microstructure and individual phase properties on the overall mechanical behavior of heterogeneous binding materials, such as cementitious pastes, targeted in this study.

Two-Way Linked Multiscale Model

In this study, two-way linked multiscale modeling is implemented to simulate fracture-associated behavior of a heterogeneous medium, i.e., geopolymer paste. A detailed review and formulation for two-way linked multiscale modeling are given in the literature (Allen 2001; Souza 2009; Kim et al. 2013), and therefore, only a brief introduction to this method is presented here. This method is entirely based on the postulate of statistical homogeneity of a composite. A general mathematical definition of statistically homogeneous media is presented in the literature (Beran and Pytte 1968), but for the current purpose, it means that the overall effective properties of a mixture are equal to the volume average of those properties over a finite representative volume element (RVE) of that mixture, provided that the size of the RVE is sufficiently large (Hashin 1983; Allen 2001). Therefore, merely the material properties and the fracture-associated properties of each individual constituent at local scale need to be known. This solution, however, is valid only if the two length scales are widely separated (Hill 1972).

By using this approach, a composite material can be simulated in two separate length scales: global scale and local scale (RVE scale of the global body). The effective (average) constitutive behavior of the composite used at the global scale is defined as the relation between the averages of field variables, i.e., stress and strain, over the local-scale volume. Those can be determined by solving an initial boundary value problem (IBVP) for the RVE while it is subjected to a homogeneous boundary condition (in traction T_i or displacement u_i), which is linked to the stress or strain tensor at the corresponding location on the global scale. The boundary condition applied to the RVE must be homogeneous in order to expect statistically homogeneous field variables. For elastic bodies, either Eq. (1) or (2) can be used to obtain the homogeneous boundary condition (Hashin 1983). Also, it should be mentioned that, in this method, any stiffness reduction due to damage accumulated at the local scale is reflected in the effective tangent constitutive behavior of the global body. Therefore, in case of progressive damage or microstructural changes in the local scale, this framework should be formulated in a two-way linked and incremental form, in which at each step (1) the effective properties at the global scale are updated according to the damage state at the corresponding local RVE and (2) the boundary condition of RVE is updated according to mechanical response at the global scale (Souza 2009)

$$T_i(S) = \sigma^0_{ji} n_j \tag{1}$$

$$u_i(S) = \varepsilon^0_{ji} x_j \tag{2}$$

where σ^0_{ij} and ε^0_{ij} = constant stress and constant strain, respectively.

Global Scale

At the global scale, the mechanical IBVP is defined by a set of governing equations [conservation of linear momentum in the absence of body forces and inertial effects, Eq. (3); conservation of angular momentum, Eq. (4); strain-displacement relations without large deformation, Eq. (5); constitutive equations, Eq. (6)], boundary conditions, and initial conditions

$$\sigma^G_{ji,j} = 0 \qquad \text{in } V^G \tag{3}$$

$$\sigma^G_{ji} = \sigma^G_{ij} \qquad \text{in } V^G \tag{4}$$

$$\varepsilon^G_{ij} = \frac{1}{2}(u^G_{i,j} + u^G_{j,i}) \qquad \text{in } V^G \tag{5}$$

$$\sigma^G_{ij}(x^G_m, t) = \bar{\Omega}^{\tau=t}_{\tau=-\infty}\{\varepsilon^G_{kl}(x^G_m, \tau)\} \qquad \text{in } V^G \tag{6}$$

where σ_{ij}, ε_{ij}, and u_i = Cauchy stress tensor, infinitesimal strain tensor, and displacement vector, respectively, at a certain location

x_i^G on the global scale at a certain time t. $\bar{\Omega}_{\tau=-\infty}^{\tau=t}$ represents the constitutive behavior at the location of x_m^G on the global scale.

Local Scale

As mentioned earlier, the global scale's effective constitutive properties are derived from the behavior of the local-scale RVE. The effective properties can be calculated from the state variables (stress and strain) derived from solving the RVE's IBVP under homogenous displacement boundary condition. For each RVE, the homogeneous displacement boundary condition is linked to the strain tensor at the corresponding location on the global scale. Similar to the global scale, the IBVP at the local scale is defined by the following governing equations

$$\sigma_{ji,j}^L = 0 \qquad \text{in } V^L \tag{7}$$

$$\sigma_{ji}^L = \sigma_{ij}^L \qquad \text{in } V^L \tag{8}$$

$$\varepsilon_{ij}^L = \frac{1}{2}(u_{i,j}^L + u_{j,i}^L) \qquad \text{in } V^L \tag{9}$$

$$\sigma_{ij}^L(t) = \bar{\Omega}_{\tau=-\infty}^{\tau=t}\{\varepsilon_{kl}^L(\tau)\} \qquad \text{in } V^L \tag{10}$$

where all variables used here are the same as those used in the global scale, except the superscript L represents the local scale.

At both the local and global scales, the material is assumed to be isotropic linear elastic, for which the stress–strain relationship is given as

$$\sigma_{ij} = \frac{E\nu}{(1+\nu)(1-2\nu)}\delta_{ij}\varepsilon_{kk} + \frac{E}{1+\nu}\varepsilon_{ij} \qquad \text{in } V \tag{11}$$

where E and ν = Young's modulus and Poisson's ratio; and δ_{ij} = Kronecker delta.

In this study, evolving damage is taken into account by allowing for microcrack growth at the local-scale RVE. Crack initiation and propagation are modeled by the linear decay cohesive zone model (Fig. 1). Among many other cohesive zone models, this study adopted the linear decay model because it can successfully simulate brittle fracture while only two cohesive zone properties are necessary to model the fracture behavior (Zhou et al. 2005; Qiao and Chen 2008). In a linear decay model the fracture energy for each mode of fracture is defined by

$$G_i = \frac{t_i^c \delta_i^c}{2} \tag{12}$$

where t_i^c and δ_i^c = critical traction and critical opening displacement, respectively. The subscript indicates the local coordinate system along with the crack opening (i = normal opening or tangential opening).

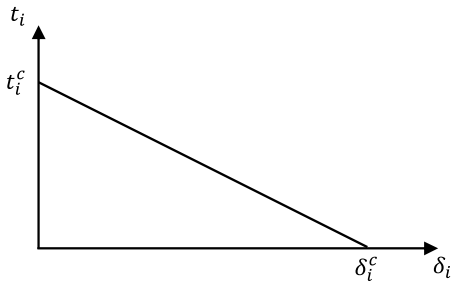

Fig. 1. Linear decay cohesive zone model.

Homogenization

As described earlier, the two-way linked multiscale modeling used here is basically a recursive scheme, in which the global-scale strain tensor is related to the local-scale displacement boundary condition, and the stiffness tangent tensor in the global scale is linked to the effective stiffness tensor from solving the IBVP for the RVE. The effective stiffness tensor is defined as the relationship between the homogenized stress and strain field over the RVE

$$\bar{\sigma}_{ij}^L = C_{ijkl}^* \bar{\varepsilon}_{kl}^L \tag{13}$$

$$\bar{\varepsilon}_{ij}^L = S_{ijkl}^* \bar{\sigma}_{kl}^L \tag{14}$$

Because the mixture is assumed to be statistically homogeneous, the volume averaging method is applicable to homogenize the field variables over RVE

$$\varepsilon_{ij}^G = \bar{\varepsilon}_{ij}^L = \frac{1}{V^L}\int_{V^L} \varepsilon_{ij}^L dV \tag{15}$$

$$\sigma_{ij}^G = \bar{\sigma}_{ij}^L = \frac{1}{V^L}\int_{V^L} \sigma_{ij}^L dV \tag{16}$$

where $\bar{\sigma}_{ij}^L$ and $\bar{\varepsilon}_{ij}^L$ = volume average of the stress and strain tensor over the RVE, respectively.

By using the divergence theorem, Eqs. (15) and (16) can be rewritten as follows:

$$\varepsilon_{ij}^G = \bar{E}_{ij}^L + \bar{e}_{ij}^L$$
$$\bar{E}_{ij}^L = \frac{1}{V^L}\int_{\partial V_E^L} \frac{1}{2}(u_i^L n_j^L + u_j^L n_i^L) dS \tag{17}$$

$$\bar{e}_{ij}^L = \frac{1}{V^L}\int_{\partial V_I^L} \frac{1}{2}(u_i^L n_j^L + u_j^L n_i^L) dS$$
$$\sigma_{ij}^G = \bar{\sigma}_{ij}^L = \frac{1}{V^L}\int_{\partial V_E^L} \sigma_{ij}^L n_k^L x_j^L dV \tag{18}$$

where $\bar{E}_{ij}^L$ and $\bar{e}_{ij}^L$ = volume averaged strain over the external (∂V_E^L) and internal (∂V_I^L) boundaries in RVE, respectively. The n_i^L is the outward unit normal vector to the external and internal boundaries. External boundaries are the RVE's outer boundaries. Internal boundaries are free surface due to new opening within the RVE as cohesive elements were created and separated.

It should be mentioned that the internal boundaries are due to developing cracks (free surfaces) inside the RVE, which implies the averaged measure of damage. Also, regarding Eq. (18), the volume averaged stress is equal to the external boundary averaged traction vectors only if the traction vector over the internal boundary surfaces is zero (Souza 2009).

Materials and Laboratory Tests

Materials and Geopolymer Sample Preparation

Low-calcium Class F fly ash was used in this study as an aluminosilicate source material to manufacture the geopolymer binder. Class F fly ash is produced from the combustion of pulverized bituminous or lignite coal, and its chemical composition is shown in Table 1. The specific gravity of the fly ash is 2.37.

The alkaline activator solution used in this study was a combination of sodium hydroxide and sodium silicate solutions. Sodium hydroxide solution of 12 molar concentration was prepared by

Table 1. Chemical composition of Class F fly ash used in this study

Component	Percentage
SiO_2	51.82
Al_2O_3	23.07
Fe_2O_3	13.02
CaO	2.79
MgO	0.85
SO_3	1.23
Na_2O	0.71
K_2O	2.52
Loss on ignition	2.41

dissolving sodium hydroxide pellets with a purity of 98% in distilled water. Sodium silicate solution with 28% SiO_2, 9% Na_2O, and 63% water was chosen for this study. The mass ratio of sodium silicate to sodium hydroxide solutions was kept constant at 1.0. The alkali solution was allowed to equilibrate for a minimum of 24 h at room temperature prior to use.

The geopolymer paste was prepared by mechanically mixing fly ash with alkaline solution in a mass ratio of 0.4 (alkali solution to fly ash). A group of beam specimens with dimensions of 160 × 40 × 40 mm (length × thickness × width) was prepared by pouring geopolymer paste into the mold in two layers and compacting using a rubber tamper. The specimens were cured at 60°C for 24 h in a laboratory oven under sealed conditions (Demie et al. 2013). The specimens were then demolded and stored in a controlled room at 20°C until the day of testing.

Global-Scale Test

A three-point bending test was conducted by placing the testing specimens on top of two rollers with a 120-mm span, as shown in Fig. 2. To ensure the centricity of the specimen during testing, an additional fixture was used to guarantee alignment of the notch with the top cross-head. The test was displacement-controlled and was conducted at a constant rate of 0.001 mm/s. Prior to testing, a small contact load of 5 N was applied, and then the test was initiated and the load–displacement data were recorded.

Local-Scale Test

To produce microstructural images of geopolymer paste, a SEM was used in the high vacuum and backscattered electron (BSE) mode. A thin coating of carbon was applied on the specimen surface before SEM imaging. The carbon coating serves to dissipate excess charge from the specimen without affecting the image contrast and interference with elements of interest (Lane 2004). BSE is one of the most commonly used imaging modes in SEM with high-energy electrons that are scattered on the sample. The contrast of the BSE images, a function of the average atomic number of the local area of the sample, was observed by different grey levels in the image (Scrivener 2004). In cementitious materials, using BSE can represent microstructural variations by separating pores and cracks from different solid phases, which will appear in darker and brighter areas in the image, respectively.

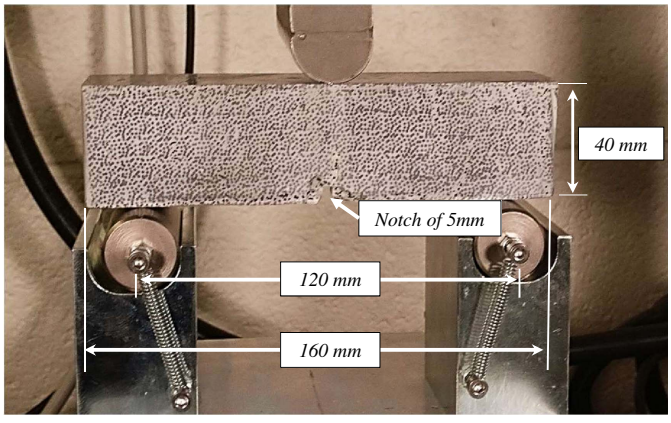

Fig. 2. Three-point bending test configuration.

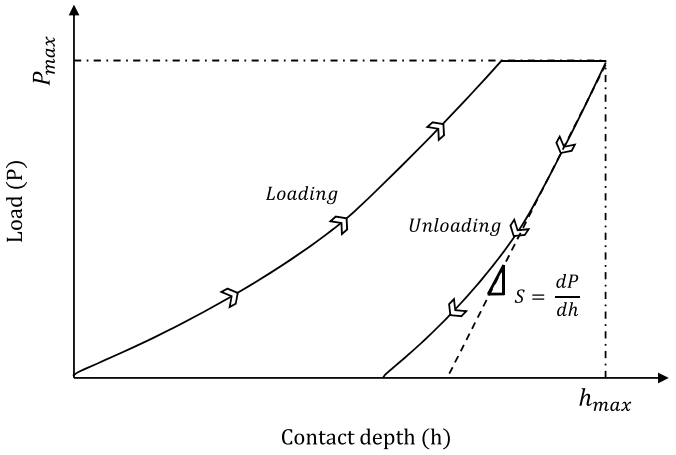

Fig. 3. Load–displacement curve from nanoindentation test.

To determine the nanomechanical properties of the geopolymer paste, a nanoindentor instrument with a Berkovich tip was used. In the indentation test, a pyramid-shaped tip (i.e., the Berkovich tip) with defined dimensions penetrates the specimen surface while the penetration depth h and the indentation load P are measured as a function of time. A schematic typical load versus displacement curve as a response of materials under applied load is presented in Fig. 3.

A quasi-static load-controlled mode was applied on the polished geopolymer paste specimens with a constant rate of 200 μN/s reaching a maximum load of 2,000 μN. The peak load was kept constant for 5 s to eliminate the effects of any possible creep (Němeček 2009). The unloading part had the same rate as the loading part and lasted for 10 s. The indentation modulus or reduced modulus (E_r) can be obtained from the following equation:

$$E_r = \frac{S}{2\beta}\sqrt{\frac{\pi}{A_c}} \tag{19}$$

where β = dimensionless correction factor that accounts for the shape of the indenter tip, which is 1.081 for Berkovich tips (Pichler and Lackner 2009); S = slope of the unloading part of the load versus displacement curve; and A_c = projected contact area, which can be extrapolated from the indentation depth h using the Oliver and Pharr method (Oliver and Pharr 1992).

Finally, the absolute elastic modulus (E_s) that is solely responsible for the unloading process can be determined by obtaining the reduced modulus (E_r) and the elastic modulus of the indenter tip (E_i). This relationship is given by

$$\frac{1}{E_r} = \frac{1-\nu_s^2}{E_s} + \frac{1-\nu_i^2}{E_i} \tag{20}$$

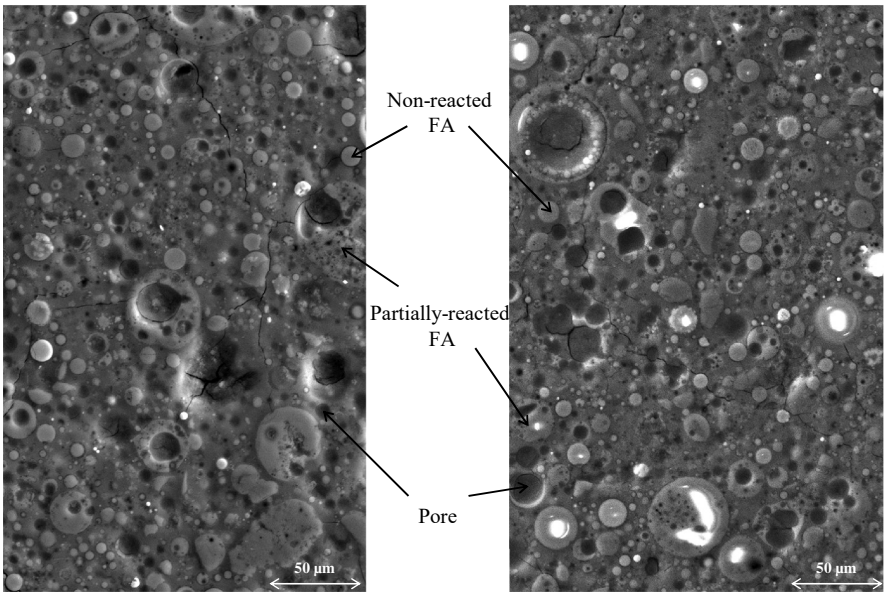

Fig. 4. BSE images of geopolymer paste.

where ν_s and ν_i = Poisson's ratios of the testing specimen and indenter tip, respectively. The Poisson's ratio of all phases within the geopolymer mixture was assumed as 0.2 (Němeček et al. 2011).

Local-Scale Test Results

As mentioned earlier, in the multiscale approach, the constitutive behavior of the heterogeneous material is derived from the behavior of the RVE. To construct the RVE, the microstructure of the heterogeneous media and properties of individual phases are necessary. Fig. 4 shows typical microstructures (BSE images) of geopolymer paste in the vicinity of aggregate particles.

It has been widely reported that a geopolymeric system, as a result of the reaction of Class F fly ash with alkali-activated solution, can be simplified as a multiphase material in which nonreacted and partially reacted fly ash phases are dispersed in an amorphous to semicrystalline matrix (i.e., alkali aluminosilicate gel also referred to as N-A-S-H gel) (Shi et al. 2012; Bakharev 2005; Das et al. 2015; Bagheri et al. 2017). Also, there are some pores (shown in darker circles) left in the N-A-S-H gel from mixing and reaction process in addition to hollow sphere fly ash particles (Shi et al. 2012).

SEM images of the geopolymer paste were used to construct the RVE microstructures. Each phase was distinguished based on color intensity by using an in-house image processing application. To capture more identifiable two-dimensional (2D) microstructures, SEM images were taken from the plane polished surface of the samples. However, in some cases, it was hard to differentiate the partially reacted fly ash from either N-A-S-H or nonreacted fly ash. Collating SEM images along with the nanoindentation results resulted in a subjective rule to distinguish the partially reacted phase from the N-A-S-H gel. Both nonreacted and partially reacted fly ash phases are usually found to be lighter in color than N-A-S-H in SEM images. The partially reacted fly ash phase, in comparison to nonreacted fly ash, usually has an irregular shape with a pitted surface appearance (as demonstrated in Fig. 4).

The nanomechanical elastic properties were obtained for each phase in geopolymer paste using the nanoindentation test. Because the elastic property of each phase was not constant with respect to the indentation location, the test was performed in multiple locations. The mean value and standard deviation of the elastic modulus resulting from at least 30 different locations of N-A-S-H gel, partially reacted, and nonreacted fly ash are presented in Table 2. Similar to other relevant studies, the nonreacted fly ash and N-A-S-H gel presented the highest and lowest stiffness values, whereas the stiffness of the partially reacted fly ash phase lies in between (Das et al. 2015).

Computational Model Simulation

The first step in implementation of the homogenization theory is to define the RVE dimension such that the overall (average) properties of the heterogeneous media are equivalent to the average properties obtained from the RVE. One widely used method to define the size of the RVE is to use statistical measures to determine the condition of statistical homogeneity (Beran 2001), such as reaching convergence of effective homogenized properties of RVE, as Hill (1972) suggested. To obtain the average stiffness of RVE, a simple tension test simulation was performed on four square trial RVEs with increasing size. Each trial RVE was finite-element meshed, as shown in Fig. 5, by using the SEM image in which four different phases are defined based on the process explained in the previous section.

The average stiffness plotted as a function of trial RVE size is shown in Fig. 5(b). The smallest size beyond which the resulting graph does not depend on the RVE size is the critical (optimum) size of RVE (Harper et al. 2012). As shown in Fig. 5(b), there was a big change from 100×100 μm to 150×150 μm, and the difference between 150×150 μm and 200×200 μm was not huge. Although no asymptotic convergence could be ascertained from the result, the 200×200 μm RVE, which is the maximum available

Table 2. Elastic moduli of individual phases from nanoindentation testing

Phase	Average E (GPa)	SD (GPa)
Phase 1 (N-A-S-H gel)	21	4.3
Phase 2 (partially reacted FA)	35	6.4
Phase 3 (nonreacted FA)	66	9.8

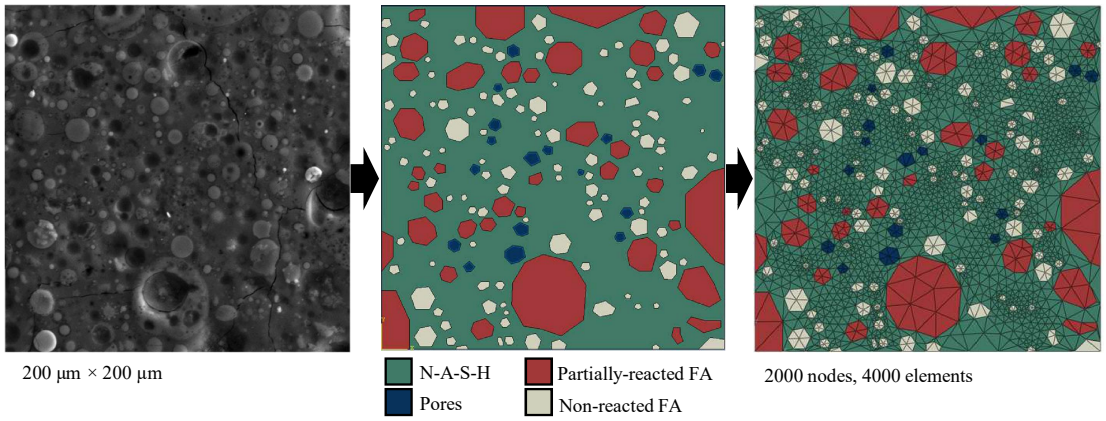

Fig. 5. (a) Finite-element mesh of microstructure; and (b) RVE size investigation.

image size, was reasonably assumed as a RVE. This limitation can be resolved by conducting a more comprehensive RVE size sensitivity study (Kim et al. 2009, 2010).

To conduct the two-way linked multiscale simulation, the three-point bend beam, as a global scale, was modeled using linear triangle elements (Tirado et al. 2017; Bozorgzad et al. 2018). Based on physical observations from the specimens tested, it was reasonably assumed that the crack nucleates and propagates only through the midline of the three-point bend specimen (i.e., the red zone in Figs. 6 and 7). It means that other parts of the specimen do not experience fracture. Therefore, the equivalent homogenized stiffness of the geopolymer bulk elements are equal to the averaged stiffness of the undamaged geopolymer paste RVE (shown in Fig. 6). The initial (intact) homogenized stiffness of the geopolymer bulk elements was calculated over the RVE using Eq. (13) under the condition in which no cohesive zone is allowed. On

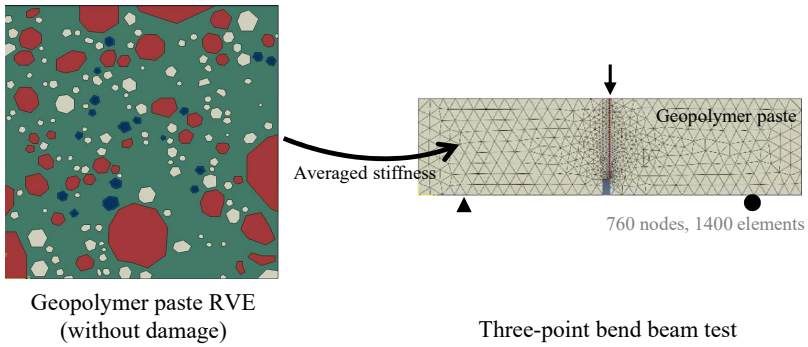

Fig. 6. Three-point bending beam model in which the bulk geopolymer elements are one-way linked to geopolymer paste RVE without damage/fracture.

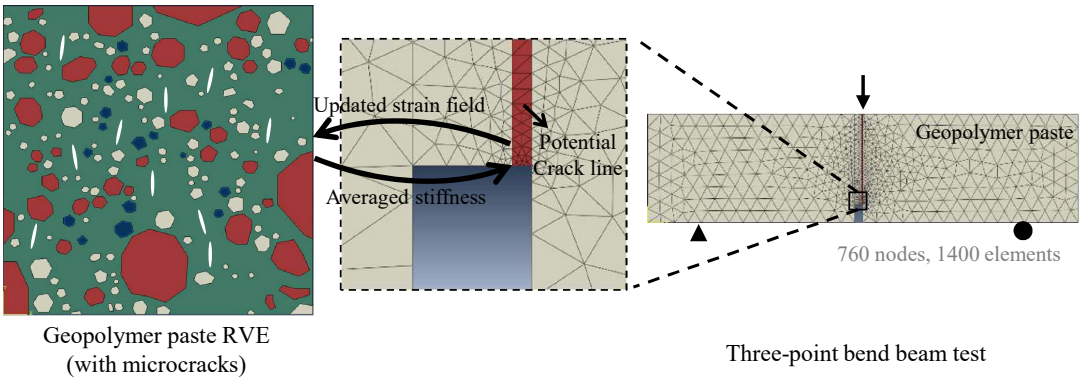

Fig. 7. Three-point bending beam model in which the cracking zone is two-way linked to geopolymer paste RVE with growing damage/fracture.

the other hand, the midline bulk elements along the potential crack zone (the elements in the potential crack line in Fig. 7) are two-way linked to the geopolymer RVE that is associated with cohesive zone creation and growth for damage initiation and fracture. The two-way linked multiscale method thus allows for stiffness reduction due to microcracking in RVE, which is consequently reflected in the global-scale behavior in a form of reduced stiffness. Cohesive zone modeling in this study allows cracks to initiate and grow only between bulk elements in the RVEs, unlike the extended finite-element method (XFEM), in which cracks can grow through the bulk elements. To minimize this limitation, cohesive zones were created (embedded) adaptively within the mesh, and the mesh structure was defined through a mesh sensitivity analysis, so that initiation of cohesive zone and its growth for crack propagation is not sensitively dependent on mesh size and mesh structure built. A finer mesh results in a higher computational cost; hence, the linear triangular element was used in this study to balance computational efficiency and modeling accuracy.

Because each element within the cracking zone will experience different deformations during the course of the simulation, each element must be linked to its corresponding RVE over which an IBVP will be solved. Hence, because the number of global elements, which are linked to the local-scale RVE, significantly affects the computational efficiency, the total number of elements linked to the local-scale RVE was limited to 60 elements in the modeling of this study.

Model Simulation Results and Discussion

To characterize the fracture properties of the geopolymer paste, the three-point bend beam test results were incorporated with the two-way linked multiscale computational modeling. In this process, the equivalent homogenized properties in the global scale (three-point bend beam) are linked to the local-scale model (i.e., geopolymer paste RVE). The two-way coupled multiscale modeling requires only the mechanical properties (i.e., elastic properties of the individual phases and fracture properties of the phases subjected to cracking) of geopolymer paste RVE as model inputs; the fracture properties can be characterized through a calibration process by comparing model simulation results and test results when others properties, except the fracture properties, are known/given.

The previously described approach works well when the nanomechanical elastic properties obtained from the nanoindentation test yield the true mechanical properties of each phase in the RVE microstructure; however, our preliminary simulation results showed that this was not the case. The load–displacement response of the three-point bend beam testing form experiment and numerical simulation are compared in Fig. 8. The dashed line represents the simulation result obtained by using the nanoindentation elastic properties of each phase (shown in Table 2). As can be seen, there is a significant difference within the initial part of the graph, which is considered to be primarily governed by the elastic properties of the individual phases, between the simulation result and its corresponding test result (in grey circles). The simulation yields an average stiffness of 25 GPa for the geopolymer paste, whereas the test result corresponds to a value of 1.5 GPa. Several factors such as simplification of real 3D microstructure into a 2D RVE microstructure might be attributed to this inconsistency, although the exact reasons are not clear at this stage. One of the major factors considered is the presence of pre-existing microcracks in the N-A-S-H gel, which are clearly observed in the SEM images as demonstrated in Figs. 4 and 9. The microcracks were developed during the curing process, and it is considered shrinkage cracking of the N-A-S-H gel from geopolymerization. The nanoindentation test could not account for the effects of these pre-existing microcracks because the testing is in the penetration (indentation) mode and the affected area of each indent is relatively very small (a few micrometers). To account for the effects of the pre-existing microcracks in the N-A-S-H gel, modified N-A-S-H gel properties were calibrated by using an analytical micromechanics approach (Hashin 1983) that addresses the reduced stiffness of the matrix phase due to the pre-existing inclusions. The solid line shown in Fig. 8 is an outcome of the modeling to estimate the modified N-A-S-H property (i.e., stiffness of 0.85 GPa).

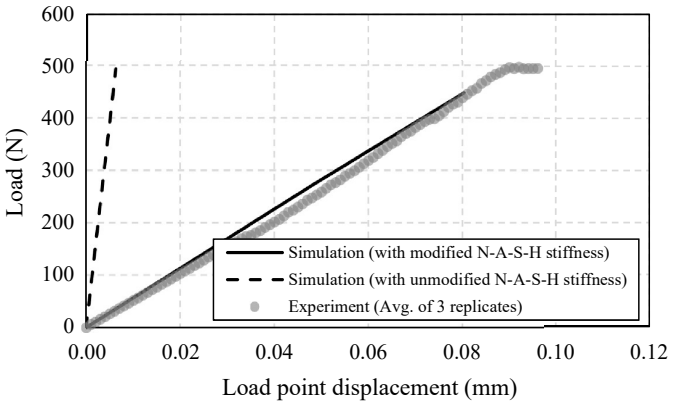

Fig. 8. Three-point bending beam response: experiment versus simulation.

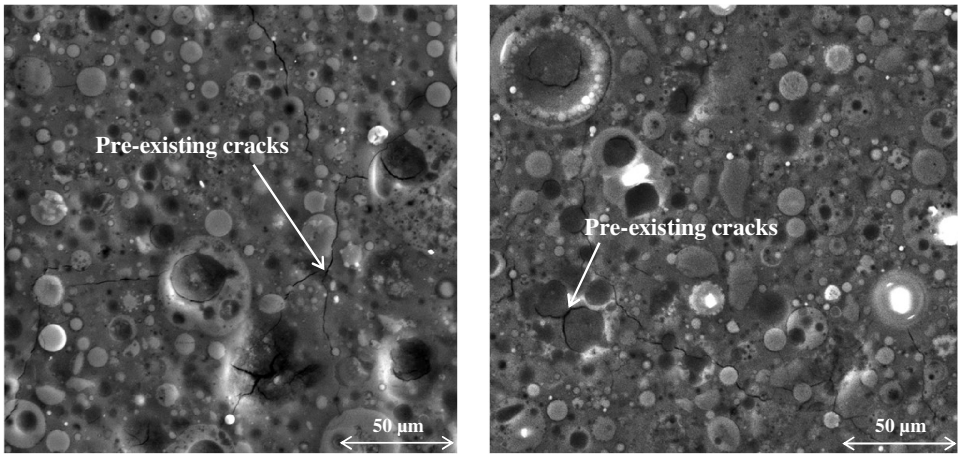

Fig. 9. SEM images of pre-existing microcracks within the N-A-S-H gel.

With the modified N-A-S-H gel property, two-way coupled multiscale modeling was redone, this time until onset of three-point bend beam fracture, to identify the fracture properties of the geopolymer paste. As described earlier, the fracture of the three-point bend beam is achieved by linking the midline cracking zone to the corresponding paste RVE microstructure (global-to-local linking), and cracking in the RVE due to progressive loading is homogenized to update the effective properties of the corresponding global-scale element (local-to-global linking). The linear decay cohesive zone model defined by the two model parameters (i.e., critical traction t_i^c and critical opening displacement δ_i^c), as shown in Fig. 1, can then be identified by the model calibration process. To reduce the modeling complexity at this stage, two assumptions were made. First, microcracks nucleate and propagate within the N-A-S-H gel and along the boundaries between N-A-S-H gel and other phases. This assumption is based on the physical observation (Fig. 9) and is also reported in other studies (Shi et al. 2012). Second, cohesive fracture properties within the N-A-S-H gel are assumed to be the same as the adhesive fracture properties between the N-A-S-H gel and other phases. This assumption is not based on any experimental measurements at this stage but made for simplicity, and it needs further examination. With the two assumptions made, only two unknown parameters describing the cohesive-adhesive fracture properties of N-A-S-H gel remain. Fig. 10 shows comparison between the test results and the multiscale model simulation results after the model calibration was completed. In the figure, two fracture properties of N-A-S-H gel are also shown.

Simulation results are also represented in a form of snapshots for both global beam specimen and local RVE microstructures. Snapshots taken at three different stages (5, 45, and 90 s) are shown in Fig. 11. The global beam results are presented in a contour plot of horizontal stress components σ_{xx}. The critical local RVE located at the tip of the notch was selected, and its deformation characteristics with cohesive zone development are presented in the figure. As shown, in the initial stage of the testing [Fig. 11(a)], the stress state in the RVE is lower than the critical traction; thus, no cohesive element is developed. By increasing the strain, the stress state in the RVE reaches a level at which cohesive zone elements develop [represented as black solid lines in Fig. 11(b)]. When a cohesive zone opening reaches the critical opening displacement, a crack develops

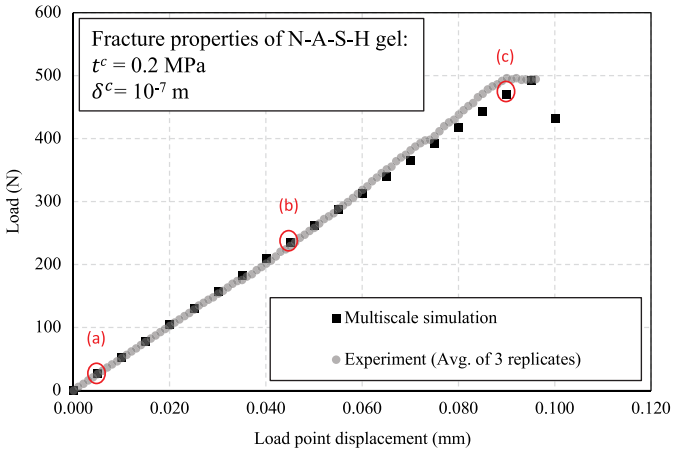

Fig. 10. Three-point bending beam response: experiment versus multiscale simulation.

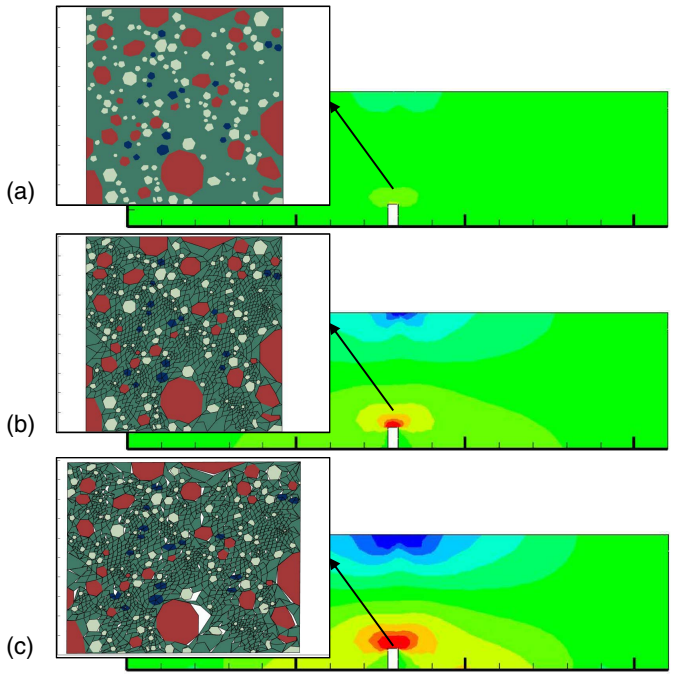

Fig. 11. Snapshots of global-local contour plots at three different loading stages: (a) $T = 5$ s; (b) $T = 45$ s; and (c) $T = 90$ s.

fully and an internal boundary forms [represented as openings in Fig. 11(c)]. Creation of internal boundaries results in loss of effective stiffness of RVE. As the simulation continues, more microcracks develop in RVE until its effective stiffness reaches a value close to zero, which is assumed to be equivalent to crack initiation of the three-point bending beam specimen and its subsequent failure.

Concluding Remarks

In this study, two-way linked multiscale computation was integrated with multiscale (global-local) tests and a cohesive zone fracture model to characterize the properties of highly heterogeneous cementitious materials, such as alkali-activated geopolymers. Geopolymer paste samples were fabricated and tested in two different length scales: (1) microstructures and nanomechanical properties of individual components within the paste in the local scale and (2) a three-point bending beam fracture test in the global scale. Local–global results were then integrated with the two-way coupled finite-element modeling in which local RVEs are allowed to develop crack initiation–propagation that is represented by the cohesive zone fracture model. Elastic properties of each phase in the microstructure RVE were obtained from the nanomechanical test, whereas fracture properties of N-A-S-H gel were estimated through a model calibration process. Based on the tests and simulation results, the following conclusions can be drawn:

- The two-way linked multiscale computation integrated with multiscale experimental tests, although it has many limitations at this stage, can be used as a method for characterization and design of various multiphase media.
- The integrated experimental–computational multiscale approach provided material properties, such as micrometer-length-scale cohesive zone fracture properties, which are considered core properties but not usually feasible to identify using conventional test methods.
- Fly ash–based geopolymer paste showed a highly complicated microstructure in which at least four different phases exist. The resulting geopolymerization phase, N-A-S-H gel, develops cracks within the gel and along the boundaries between the gel and other phases, such as fly ash particles with different levels of reaction with alkaline solution.

Acknowledgments

The authors gratefully acknowledge the National Science Foundation (CMMI-1635055) for their financial support to accomplish this research.

References

Allen, D. H. 2001. "Homogenization principles and their application to continuum damage mechanics." *Compos. Sci. Technol.* 61 (15): 2223–2230. https://doi.org/10.1016/S0266-3538(01)00116-6.

Allison, P. G., C. A. Weiss, R. D. Moser, A. J. Diaz, O. G. Rivera, and S. S. Holton. 2015. "Nanoindentation and SEM/EDX characterization of the geopolymer-to-steel interfacial transition zone for a reactive porcelain enamel coating." *Compos. Part B* 78: 131–137. https://doi.org/10.1016/j.compositesb.2015.03.011.

Bagheri, A., A. Nazari, J. G. Sanjayan, and P. Rajeev. 2017. "Alkali activated materials vs geopolymers: Role of boron as an eco-friendly replacement." *Constr. Build. Mater.* 146: 297–302. https://doi.org/10.1016/j.conbuildmat.2017.04.137.

Bakharev, T. 2005. "Geopolymeric materials prepared using Class F fly ash and elevated temperature curing." *Cem. Concr. Res.* 35 (6): 1224–1232. https://doi.org/10.1016/j.cemconres.2004.06.031.

Beran, M. J. 2001. "Statistical continuum mechanics." In *Mechanics of random and multiscale microstructures*, edited by D. Jeulin and M. Ostoja-Starzewski, 1–31. New York: Springer.

Beran, M. J., and A. Pytte. 1968. "Statistical continuum theories." *Am. J. Phys.* 36 (10): 923. https://doi.org/10.1119/1.1974326.

Bleszynski, R. F., and M. D. Thomas. 1998. "Microstructural studies of alkali-silica reaction in fly ash concrete immersed in alkaline solutions." *Adv. Cem. Based Mater.* 7 (2): 66–78. https://doi.org/10.1016/S1065-7355(97)00030-8.

Bozorgzad, A., S. F. Kazemi, and F. Moghadas Nejad. 2018. "Finite-element modeling and laboratory validation of evaporation-induced moisture damage to asphalt mixtures." In *Proc., 97th Transportation Research Board Annual Meeting*. Washington, DC: Transportation Research Board.

Broughton, J. Q., F. F. Abraham, N. Bernstein, and E. Kaxiras. 1999. "Concurrent coupling of length scales: Methodology and application." *Phys. Rev. B* 60 (4): 2391–2403. https://doi.org/10.1103/PhysRevB.60.2391.

Das, S., P. Yang, S. S. Singh, J. C. Mertens, X. Xiao, N. Chawla, and N. Neithalath. 2015. "Effective properties of a fly ash geopolymer: Synergistic application of X-ray synchrotron tomography, nanoindentation, and homogenization models." *Cem. Concr. Res.* 78 (Dec): 252–262. https://doi.org/10.1016/j.cemconres.2015.08.004.

Da Silva, W., J. Němeček, and P. Štemberk. 2014. "Methodology for nanoindentation-assisted prediction of macroscale elastic properties of high performance cementitious composites." *Cem. Concr. Compos.* 45 (Jan): 57–68. https://doi.org/10.1016/j.cemconcomp.2013.09.013.

Demie, S., M. F. Nuruddin, and N. Shafiq. 2013. "Effects of micro-structure characteristics of interfacial transition zone on the compressive strength of self-compacting geopolymer concrete." *Constr. Build. Mater.* 41 (Apr): 91–98. https://doi.org/10.1016/j.conbuildmat.2012.11.067.

Hain, M., and P. Wriggers. 2008. "Numerical homogenization of hardened cement paste." *Comput. Mech.* 42 (2): 197–212. https://doi.org/10.1007/s00466-007-0211-9.

Harper, L. T., C. Qian, T. A. Turner, S. Li, and N. A. Warrior. 2012. "Representative volume elements for discontinuous carbon fibre composites. Part 2: Determining the critical size." *Compos. Sci. Technol.* 72 (2): 204–210. https://doi.org/10.1016/j.compscitech.2011.11.003.

Hashin, Z. 1983. "Analysis of composite materials." *J. Appl. Mech.* 50 (3): 481–505. https://doi.org/10.1115/1.3167081.

Hill, R. 1972. "On constitutive macro-variables for heterogeneous solids at finite strain." *Proc. R. Soc. London A* 326 (1565): 131–147. https://doi.org/10.1098/rspa.1972.0001.

Karamnejad, A., V. P. Nguyen, and L. J. Sluys. 2013. "A multi-scale rate dependent crack model for quasi-brittle heterogeneous materials." *Eng. Fract. Mech.* 104 (May): 96–113. https://doi.org/10.1016/j.engfracmech.2013.03.009.

Karamnejad, A., and L. J. Sluys. 2014. "A dispersive multi-scale crack model for quasi-brittle heterogeneous materials under impact loading." *Comput. Methods Appl. Mech. Eng.* 278: 423–444. https://doi.org/10.1016/j.cma.2014.05.020.

Khedmati, M., Y. R. Kim, J. A. Turner, H. Alanazi, and C. Nguyen. 2018. "An integrated microstructural-nanomechanical-chemical approach to examine material-specific characteristics of cementitious interphase regions." *Mater. Charact.* 138 (Apr): 154–164. https://doi.org/10.1016/j.matchar.2018.01.045.

Kim, Y., J. Lee, and J. Lutif. 2010. "Geometrical evaluation and experimental verification to determine representative volume elements of heterogeneous asphalt mixtures." *J. Test. Eval.* 38 (6): 660–666.

Kim, Y., J. S. Lutif, and D. H. Allen. 2009. "Determining representative volume elements of asphalt concrete mixtures without damage." *Transp. Res. Rec.* 2127: 52–59. https://doi.org/10.3141/2127-07.

Kim, Y., F. V. Souza, and J. E. S. L. Teixeira. 2013. "A two-way coupled multiscale model for predicting damage-associated performance of asphaltic roadways." *Comput. Mech.* 51 (2): 187–201. https://doi.org/10.1007/s00466-012-0716-8.

Lane, D. S. 2004. *Petrographic methods of examining hardened concrete*. FHWA-HRT-04-150. Washington, DC: USDOT.

Lecomte, I., C. Henrist, M. Liegeois, F. Maseri, A. Rulmont, and R. Cloots 2006. "(Micro)-structural comparison between geopolymers, alkali-activated slag cement and portland cement." *J. Eur. Ceram. Soc.* 26 (16): 3739–3789.

Menčík, J., L. H. He, and J. Němeček. 2011. "Characterization of viscoelastic-plastic properties of solid polymers by instrumented indentation." *Polym. Test.* 30 (1): 101–109. https://doi.org/10.1016/j.polymertesting.2010.11.006.

Mondal, P., S. P. Shah, and L. D. Marks. 2008. "Nanoscale characterization of cementitious materials." *ACI Mater. J.* 105 (2): 174–179.

Mouret, M., A. Bascoul, and G. Escadeillas. 1999. "Microstructural features of concrete in relation to initial temperature—SEM and ESEM characterization." *Cem. Concr. Res.* 29 (3): 369–375. https://doi.org/10.1016/S0008-8846(98)00160-4.

Němeček, J. 2009. "Creep effects in nanoindentation of hydrated phases of cement pastes." *Mater. Charact.* 60 (9): 1028–1034. https://doi.org/10.1016/j.matchar.2009.04.008.

Němeček, J., V. Šmilauer, and L. Kopecký. 2009. "Characterization of alkali-activated fly-ash by nanoindentation." *Nanotechnol. Constr.* 3: 337–343.

Němeček, J., V. Šmilauer, and L. Kopecký. 2011. "Nanoindentation characteristics of alkali-activated aluminosilicate materials." *Cem. Concr. Compos.* 33 (2): 163–170. https://doi.org/10.1016/j.cemconcomp.2010.10.005.

Nguyen, V. P., M. Stroeven, and L. J. Sluys. 2012. "Multiscale failure modeling of concrete: Micromechanical modeling, discontinuous homogenization and parallel computations." *Comput. Methods Appl. Mech. Eng.* 201: 139–156. https://doi.org/10.1016/j.cma.2011.09.014.

Oliver, W. C., and G. M. Pharr. 1992. "An improved technique for determining hardness and elastic modulus using load and displacement sensing indentation experiments." *J. Mater. Res.* 7 (6): 1564–1583. https://doi.org/10.1557/JMR.1992.1564.

Pelisser, F., E. L. Guerrino, M. Menger, M. D. Michel, and J. A. Labrincha. 2013. "Micromechanical characterization of metakaolin-based geopolymers." *Constr. Build. Mater.* 49 (Dec): 547–553. https://doi.org/10.1016/j.conbuildmat.2013.08.081.

Pichler, C., and R. Lackner. 2009. "Upscaling of viscoelastic properties of highly-filled composites: Investigation of matrix-inclusion-type morphologies with power-law viscoelastic material response." *Compos. Sci. Technol.* 69 (14): 2410–2420. https://doi.org/10.1016/j.compscitech.2009.06.008.

Qian, Z., G. Ye, E. Schlangen, and K. van Breugel. 2011. "3D lattice fracture model: Application to cement paste at microscale." *Key Eng. Mater.* 452–453: 65–68. https://doi.org/10.4028/www.scientific.net/KEM.452-453.65.

Qiao, P., and Y. Chen. 2008. "Cohesive fracture simulation and failure modes of FRP-concrete bonded interfaces." *Theor. Appl. Fract. Mech.* 49 (2): 213–225. https://doi.org/10.1016/j.tafmec.2007.11.005.

Sakulich, A. R., and V. C. Li. 2011. "Nanoscale characterization of engineered cementitious composites (ECC)." *Cem. Concr. Res.* 41 (2): 169–175. https://doi.org/10.1016/j.cemconres.2010.11.001.

Scrivener, K. L. 2004. "Backscattered electron imaging of cementitious microstructures: Understanding and quantification." *Cem. Concr. Compos.* 26 (8): 935–945. https://doi.org/10.1016/j.cemconcomp.2004.02.029.

Shi, X. S., F. G. Collins, X. L. Zhao, and Q. Y. Wang. 2012. "Mechanical properties and microstructure analysis of fly ash geopolymeric recycled concrete." *J. Hazard. Mater.* 237: 20–29. https://doi.org/10.1016/j.jhazmat.2012.07.070.

Škvára, F., L. Kopecký, J. Nemecek, and Z. Bittnar. 2006. "Microstructure of geopolymer materials based on fly ash." *Ceramics-Silikaty* 50 (4): 208–215.

Šmilauer, V., P. Hlaváček, F. Škvára, R. Šulc, L. Kopecký, and J. Němeček. 2011. "Micromechanical multiscale model for alkali activation of fly ash and metakaolin." *J. Mater. Sci.* 46 (20): 6545–6555. https://doi.org/10.1007/s10853-011-5601-x.

Somna, K., C. Jaturapitakkul, P. Kajitvichyanukul, and P. Chindaprasirt. 2011. "NaOH-activated ground fly ash geopolymer cured at ambient temperature." *Fuel* 90 (6): 2118–2124. https://doi.org/10.1016/j.fuel.2011.01.018.

Souza, F. V. 2009. "Multiscale modeling of impact on heterogeneous viscoelastic solids with evolving microcracks." Engineering Mechanics dissertations and theses, Univ. of Nebraska-Lincoln.

Souza, F. V., and D. H. Allen. 2010. "Multiscale modeling of impact on heterogeneous viscoelastic solids containing evolving microcracks." *Int. J. Numer. Methods Eng.* 82 (4): 464–504. https://doi.org/10.1002/nme.2773.

Souza, F. V., D. H. Allen, and Y. Kim. 2008. "Multiscale model for predicting damage evolution in composites due to impact loading." *Compos. Sci. Technol.* 68 (13): 2624–2634. https://doi.org/10.1016/j.compscitech.2008.04.043.

Tirado, C., K. Y. Gamez-Rios, A. Fathi, M. Mazari, and S. Nazarian. 2017. "Simulation of lightweight deflectometer measurements considering nonlinear behavior of geomaterials." *Transp. Res. Rec.* 2641: 58–65. https://doi.org/10.3141/2641-08.

Trtik, P., J. Kaufmann, and U. Volz. 2012. "On the use of peak-force tapping atomic force microscopy for quantification of the local elastic modulus in hardened cement paste." *Cem. Concr. Res.* 42 (1): 215–221. https://doi.org/10.1016/j.cemconres.2011.08.009.

Winnefeld, F., A. Leemann, M. Lucuk, P. Svoboda, and M. Neuroth. 2010. "Assessment of phase formation in alkali activated low and high calcium fly ashes in building materials." *Constr. Build. Mater.* 24 (6): 1086–1093. https://doi.org/10.1016/j.conbuildmat.2009.11.007.

You, T., Y. Kim, and T. Park. 2017. "Two-way coupled multiscale model for predicting mechanical behavior of bone subjected to viscoelastic deformation and fracture damage." *J. Eng. Mater. Technol.* 139 (2): 021016. https://doi.org/10.1115/1.4035618.

Zhou, F., J. F. Molinari, and T. Shioya. 2005. "A rate-dependent cohesive model for simulating dynamic crack propagation in brittle materials." *Eng. Fract. Mech.* 72 (9): 1383–1410. https://doi.org/10.1016/j.engfracmech.2004.10.011.